MACROSCOPIC DEFORMATION MODES AND STRESS PARAMETERS IN METALLIC MATERIALS AFTER LOW TEMPERATURE IRRADIATION – T. S. Byun and K. Farrell (Oak Ridge National Laboratory) and M. Li (Argonne National Laboratory)

OBJECTIVE

The objective of this work is to produce macroscopic deformation mode maps for an extended set of irradiated metallic materials and to characterize the effects of radiation on macroscopic deformation modes and true stress parameters for each material group.

SUMMARY

Macroscopic deformation modes, elastic, uniform plastic, and unstable plastic deformation modes, are mapped in tensile true stress-dose space for more than two dozen metallic materials consisting of 13 bcc, 11 fcc, and 2 hcp metals irradiated at low temperatures (≤ 200^{o}C). The boundaries between different deformation regions are set by the yield stress (YS), plastic instability stress (PIS), and true fracture stress (FS) versus dose curves. The annealed fcc metals display large uniform plasticity regions, while unstable deformation regions are dominant in the harder bcc and hcp metals. The PIS values for all materials are independent of dose except for the precipitation-hardened IN718 alloy where the irradiation-induced phase change reduces its PIS. In the bcc materials for high temperature application, such as 9Cr ferritic/martensitic steels, sintered molybdenum, vanadium, and tantalum, the radiation-induced embrittlement is characterized in terms of FS decreasing with dose at relatively high doses. The FS is nearly dose-independent below the critical dose for the embrittlement. It is concluded that the tensile stress-based deformation mode maps effectively integrate mechanical property information and characterize differences in radiation effects between crystalline structures or material groups. Also, the analysis results indicate that the low temperature irradiation does not significantly change the strain-hardening rate of metallic materials. Such a dose independence in strain hardening behavior results in strong linear relationships between the true stress parameters.

PROGRESS AND STATUS

Introduction

Irradiation of metallic materials with high energy particles at low temperatures induces formation of numerous tiny defect clusters of nanometer size or larger [1-4]. Such clusters can act as strong obstacles to dislocation glide, and therefore, the microstructural change by low temperature irradiation leads to a significant increase of strength and is usually accompanied by reduction of ductility [2-14]. This report proposes an effective way to interpret and integrate such radiation-induced changes for different classes of materials.

Mapping deformation regimes and mechanisms on a coordinate plane has been regarded as a good method of displaying highly-integrated material property information. Thus far at least two types of deformation maps have been constructed for irradiated materials: Ashby-type deformation mechanism maps on stress-temperature plane [14-19] and Okada et al's strain localization map on strain-dose plane [20,21]. The Ashby deformation map displays the fields of normalized stress and temperature in which a particular mechanism of plastic flow is dominant and is constructed focusing on high temperature deformation, i.e., creep mechanisms. This type of map has been widely used for commercial materials for high temperature applications [17-19]. Recently, Zinkle and Lucas [14] have constructed Ashby-type deformation maps for irradiated and nonirradiated face-centered cubic (fcc) and body centered cubic (bcc) metals. It was concluded that the Ashby deformation maps were useful frameworks for categorizing the effects of irradiation on mechanical behaviors. Okada et al [20] have constructed maps to express irradiation-induced changes in deformation mechanisms on engineering strain-dose plane. Their mapping was based on transmission electron microscopy (TEM) results for pure nickel and gold, and it outlined the borders for localized deformation (channeling) and uniform deformation (dislocation tangling) mechanisms. Similar deformation mechanism maps have been published recently for commercial nuclear

structural alloys such as A533B steel, 316 stainless steel, and Zircaloy-4 [21]. In [20,21] the deformation temperature was fixed at room temperature.

Since deformation mechanisms are closely related to applied stress, the microstructure-based mapping was expected to be more effectively expressed on the true stress-dose plane rather than on the engineering strain-dose plane [13,22,23]. Further, a deformation mechanism map constructed in the true stress-dose coordinate system describes well the whole macroscopic deformation process consisting of elastic, uniform plastic, and unstable plastic deformation regimes [22]. Therefore, mapping tensile deformation modes without overlaying the microscopic mechanisms on them has been attempted for selected nuclear structural materials using true stress parameters such as yield stress (YS), plastic instability stress (PIS), and true fracture stress (FS) [13,23,24]. It was confirmed that the tensile data-based macroscopic mode maps could provide well-integrated information on the macroscopic deformation modes of irradiated and nonirradiated materials [23]. In this report the macroscopic deformation mode maps are presented for extended datasets for irradiated materials, which were produced through more than three dozen irradiation experiments [25-27]. The data are analyzed and integrated into 18 deformation mode maps for individual materials. Also, detailed analyses are performed for the individual dose and stress parameters and their relationships.

Experimental

Materials and Irradiation

This report selects and analyzes 39 datasets from room temperature tensile tests after low temperature irradiations (average irradiation temperature $\leq$ 200 ^{o}C) [26-28]. Table 1 lists those 39 cases and provides corresponding specimen types and irradiation temperatures and dose ranges. Three different types of miniature tensile specimens, SS-3, S-1, and BES/NERI types, were used for the experiments and their gage section dimensions are provided in the notes in Table 1.

Irradiation experiments were performed at two facilities: the Hydraulic Tube facility of the High Flux Isotope Reactor (HFIR) at Oak Ridge National Laboratory and the target area of the Los Alamos Neutron Scattering Center (LANSCE) accelerator at Los Alamos National Laboratory. In the HFIR irradiation facility, the tensile specimens were exposed to fast neutrons (E > 0.1 MeV) for different periods to achieve target damage levels [26]. The irradiation temperature in the HFIR irradiation facility was estimated to be in the range 60-100^{o}C. For the most part, the bare specimens were in direct contact with the flowing water coolant. Those materials that undergo corrosion in water, such as Fe, Cu, Zr, Zr-4, and A533B steel, were vacuum-sealed in aluminum foil envelopes that were compressed against the specimens by the hydraulic pressure during irradiation.

In the LANSCE accelerator, the tensile specimens were irradiated at different locations in the target-area to obtain different irradiation exposures to protons and spallation neutrons [27,28]. The kinetic energy of the incident protons was 800 MeV, and spallation reactions by the protons produced neutrons with a wide range of kinetic energy ($\leq$800 MeV). The protons produced most of displacement damage in specimens located at the front positions of target in the proton beam (p>n area) while the spallation neutrons made more or similar contributions to the damage at the back positions of the target (n>p area).

Specimens in the proton-dominant area, S-1 type specimens, received higher dpa values while those in the neutron-dominant area, SS-3 type specimens, got relatively low doses (< 1 dpa). Total doses for each alloy (from protons plus neutrons) are given in the displacements per atom (dpa) column in Table 1. The maximum temperatures measured by thermocouples were in the range 50-260^{o}C during irradiation.

The chemical compositions and heat treatment procedures are summarized in references [24,27] for the tested alloys and pure metals. Several metals and alloys were used in multiple irradiation experiments in the same or different heat treatment conditions. All tensile tests were conducted at room temperature in screw-driven machines at a strain rate of about 10^{-3} sec^{-1}. Since the differences in the specimen types and in the irradiation facilities did not lead to noticeable differences in the tensile properties [10], data for each material were assembled into a single map ignoring the differences in the procedures prior to tensile testing.

Table 1. Summary of irradiation experiments

Case #	Material	Specimen Type*	Irradiation Facility**	Dose Range, dpa	Irradiation Temperature, ^{o}C
1	A533B	BES/NERI	HFIR (n)	0 – 0.89	60 -100
2	A533B	SS-3	HFIR (n)	0 – 1.28	60 -100
3	9Cr-2WVTa	S-1	LANSCE (n<p)	0 – 10.15	50 - 160
4	9Cr-2WVTa	SS-3	LANSCE (n>p)	0 – 0.12	90 - 260
5	9Cr-1MoVNb	S-1	LANSCE (n<p)	0 – 10.15	50 - 160
6	9Cr-1MoVNb	SS-3	LANSCE (n>p)	0 – 0.12	90 - 260
7	Ta-1W	BES/NERI	HFIR (n)	0 – 0.14	60-100
8	Ta-1W	S-1	LANSCE (n<p)	0 – 7.52	50 - 160
9	Ta-1W	SS-3	LANSCE (n>p)	0 – 0.08	90 - 260
10	Ta-10W	S-1	LANSCE (n<p)	0 – 25.23	50 - 160
11	Ta-10W	SS-3	LANSCE (n>p)	0 – 0.08	90 - 260
12	Fe	BES/NERI	HFIR (n)	0 – 0.79	60 -100
13	Mo (LCAC)	SS-3	HFIR (n)	0 – 0.28	60 -100
14	Mo (PM)	BES/NERI	HFIR (n)	0 – 0.07	60 -100
15	Nb	BES/NERI	HFIR (n)	0 – 0.37	60 -100
16	V	BES/NERI	HFIR (n)	0 – 0.69	60 -100
17	Ta (Aesar-1)	BES/NERI	HFIR (n)	0 – 0.14	60 -100
18	Ta (Aesar-2)	BES/NERI	HFIR (n)	0 – 0.14	60 -100
19	Ta (ISIS)	BES/NERI	HFIR (n)	0 – 0.14	60 -100
20	316	BES/NERI	HFIR (n)	0 – 0.78	60 -100
21	EC316LN	S-1	LANSCE (n<p)	0 – 10.67	50 - 160
22	EC316LN	SS-3	LANSCE (n>p)	0 – 0.12	90 - 260
23	AL6XN	S-1	LANSCE (n<p)	0 – 10.67	50 - 160
24	AL6XN	SS-3	LANSCE (n>p)	0 – 0.12	90 - 260
25	HTUPS316	S-1	LANSCE (n<p)	0 – 4.0	50 - 160
26	HTUPS316	SS-3	LANSCE (n>p)	0 – 0.12	90 - 260
27	Fe-21Ni-16Cr (R)	S-1	LANSCE (n<p)	0 – 11.28	50 - 160
28	Fe-21Ni-16Cr (S)	S-1	LANSCE (n<p)	0 – 11.28	50 - 160
29	Al 1100-0	BES/NERI	HFIR (n)	0 – 1.11	60 -100
30	Al 6061-0	S-1	LANSCE (n<p)	0 – 0.14	50 - 160
31	Al 6061-T651	S-1	LANSCE (n<p)	0 – 0.14	50 - 160
32	IN718-PH	SS-3	HFIR (n)	0 – 1.2	60 -100
33	IN718-SA	SS-3	HFIR (n)	0 – 1.2	60 -100
34	Cu	BES/NERI	HFIR (n)	0 – 0.92	60 -100
35	Ni	BES/NERI	HFIR (n)	0 – 0.6	60 -100
36	Zr-4	BES/NERI	HFIR (n)	0 – 0.8	60 -100
37	Zr-4	S-1	LANSCE (n<p)	0 – 24.58	50 - 160
38	Zr-4	SS-3	LANSCE (n>p)	0 – 0.12	90 - 260
39	Zr	BES/NERI	HFIR (n)	0 – 0.63	60 -100

*Gage section dimensions for SS-3, S-1, and BES/NERI types are 0.76 ×1.52 × 7.62, 0.25 ×1.2 × 5, and 0.25 ×1.5 × 8 mm, respectively. **Irradiation particles: (n) – fast neutron irradiation; (n<p) – high energy protons dominant in the mixture of incident protons and spallation neutrons; (n>p) - fast neutrons dominant in the mixture of incident protons and spallation neutrons. SA - solution annealed; (R) - recrystallized; (S) – single crystal; others were produced by typical heat treatments for each metal or alloy [27].

Calculation of true stress boundaries

Developing a macroscopic deformation mode map in this study is actually a process of drawing boundaries between macroscopic deformation modes based on the tensile test data. Such boundaries are set by the true stress parameters, YS, PIS, and FS, plotted as functions of dose in true stress-dose coordinate system. The methods to obtain the values of these parameters are described in this section,

along with some latest findings and explanations [22-24]. First, the lowest stress parameter YS is obtained directly from tensile test data and it sets the boundary between elastic and plastic deformation regions. It is assumed that any micro-plasticity that occurs before the yield point is within the elastic regime. Throughout this study the lower yield stress is used for the YS if a yield drop occurred; otherwise, the 0.2% elongation offset yield stress is used.

Second, the PIS (σ_{PIS} in mathematical formula) is defined as the true stress version of the ultimate tensile strength (UTS), where the onset of plastic instability (necking) occurs, and sets the boundary between the uniform and unstable plastic flow modes. It is calculated from tensile test data, UTS (= S_{UTS} in equations) and uniform plastic strain ε_U^P, using a constant volume condition for plasticity [24]:

$$\sigma_{PIS} = S_{UTS} \times \exp(\varepsilon_U^P) \qquad (1)$$

For most of the materials studied here, it has been shown that below the critical dose for necking at yield the PIS is nearly independent of dose [24]. Thus, the PIS is regarded as a material-specific constant, or a criterion for plastic instability, for a material in both its irradiated and nonirradiated conditions; the engineering tensile curve after irradiation shows necking at yield when the yield stress is above the plastic instability stress of the nonirradiated material. This criterion was also confirmed to be valid for prestrained (cold-rolled) materials; addition of dislocations at a temperature lower than test temperature did not affect the PIS value [29]. Therefore, the PIS is believed to be independent of radiation-induced defect clusters and dislocation tangles. The dose-independent PIS is not defined when the plastic instability occurs at yield (YS > PIS). The dose at the critical point (YS = PIS) is defined as the dose to plastic instability at yield, D_C [24,30], above which there is no uniform deformation region and the YS and FS curves define the region for unstable (necking) deformation mode.

Third, approximations and iterative calculations are needed to obtain the highest stress parameter, FS, unless reduction-in-area values are measured or the specimen breaks in a fully brittle mode, since the dimension of the localized neck is necessary to calculate true strain at failure. After the onset of necking the stress state at the neck becomes triaxial, and therefore, the tensile stress defined by the load (P) divided by the minimum cross-sectional area of the neck (A_n) becomes the nominal (or axial) stress component in the tensile loading direction, which differs from the effective (or equivalent) stress. The axial and equivalent stresses are identical during uniform tensile deformation [31-33]. Since the stress components in the perpendicular directions are tensile but lower than the axial component, the effective stress is slightly lower than the axial component. A linear strain-hardening model for the effective stress gives an upper limit for the true stress-true strain curve for necking deformation [32]. In the present study, the nominal stress component (P/A_n) is used for true stress, instead of using effective stress, since the nominal stress component measured at fracture is usually regarded as the true fracture stress. A comparison of PIS and average strain-hardening rate (in normal stress units) led to the conclusion that the strain-hardening rate remains nearly unchanged at the PIS level during necking deformation [29]. It was also concluded [22] that the linear stress-strain curve during necking is a satisfactory approximation for the constitutive equation of necking deformation. Note that the equivalence of these two conclusions can be simply proved by applying Considere's instability criterion to the linear strain-hardening equation at the onset of necking.

In modeling a constitutive equation for unstable deformation, it should be considered that the true stress-true strain curve starts from the higher one of the YS or PIS, and the YS can be higher than the PIS after irradiation. Then, the above finding leads to the following linear true stress-true strain relationship in the necking strain range ($\varepsilon_U^P \le \varepsilon^P \le \varepsilon_F^P$) [22,23]:

$$\sigma(\varepsilon^P) = \max(\sigma_{YS}, \sigma_{PIS}) + \sigma_{PIS}(\varepsilon^P - \varepsilon_U^P) \qquad (2)$$

where ε^P, ε_U^P, ε_F^P, σ_{YS} and σ_{PIS} are the plastic strain, the true uniform plastic strain, the plastic strain at fracture, the yield stress, and the plastic instability stress, respectively. Then, the true fracture stress, σ_{FS}, can be calculated by replacing ε^P with ε_F^P in Eq. (2),

$$\sigma_{FS} = \max(\sigma_{YS}, \sigma_{PIS}) + \sigma_{PIS}(\varepsilon_F^P - \varepsilon_U^P) \quad (3)$$

(Note that the stress parameters, σ_{YS}, σ_{PIS}, and σ_{FS}, are defined for mathematical expressions only and are identical to YS, PIS, and FS, respectively.) Also, σ_{FS} can be calculated from the engineering fracture stress S_{FS} using the constant volume condition:

$$\sigma_{FS} = S_{FS} \times \exp(\varepsilon_F^P) . \quad (4)$$

The solution for ε_F^P and σ_{FS} can be obtained by iterative calculations using Equations (3) and (4) and measured tensile data: σ_{YS}, S_{UTS}, S_{FS}, and ε_U^P.

Results and discussion

Maps for bcc materials

Figures 1(a) -1(c) display macroscopic deformation maps for bcc materials based on the dose dependencies of true stress parameters [23]. The map for A533B steel, Fig. 1(a), shows that the YS increases with dose until it nearly saturates at ~ 1000 MPa above 0.1 dpa, making the elastic deformation region larger. The PIS is almost constant in the dose range of 0 – 0.02 dpa and it intersects the YS-dose curve at about 0.02 dpa, which was defined as the critical dose D_C [24,30] for the A533B steel. The A533B map shows that the FS is nearly independent of dose in the dose range of 0 - 1.3 dpa. It has an average value of ~1300 MPa with a large scatter; there is evidence of decrease with dose, which would have been perceived as a sign of embrittlement. Since the average PIS value (~700 MPa) is only about 1.5 times the YS of nonirradiated material (~470 MPa) and the YS increases with dose to make an intercept with the PIS line, the uniform deformation region which is defined by these two parameters is relatively small. This agrees with the relatively small uniform ductility observed in this steel before irradiation (~15%). The necking deformation region is typically a few times larger than the uniform deformation region.

For the ferritic/martensitic steels, 9Cr-1MoVNb and 9Cr-2WVTa, the true stress data after irradiation in spallation conditions to higher doses up to ~10 dpa are presented in Fig. 1(b). The small gap between the YS and the PIS produced a small region for uniform plasticity. The FS varied within a range over a dose range of 0 – 0.1 dpa, while it decreased with dose from the maximum at about 0.1 dpa until it experienced a complete embrittlement (fracture before yield) at 10.2 dpa. Such a decrease in FS indicates that the materials have been partially embrittled between 1 and 10.2 dpa. Since the FS is more than two times higher than the PIS prior to the embrittlement, the unstable deformation region is much larger than the narrow uniform plasticity region. This suggests that the necking deformation in bcc metals (maybe in all hard but ductile metals) should be given more attention in embrittlement analyses.

Figure 1(c) is the deformation mode map for Ta-1W alloy after neutron or neutron plus proton irradiation. Again, the PIS and the FS are nearly independent of dose, while the YS is strongly dose dependent. The PIS and FS values of Ta-1W alloy are in the range 450 – 490 MPa and 1200 – 1300 MPa, respectively. This large difference between the PIS and FS values produced a large plastic instability region. A notable feature found in the map of Ta-1W is that the YS line is far below the FS line at the highest dose 7.5 dpa. This indicates that the Ta-1W alloy may not experience radiation-induced embrittlement until its dose reaches beyond 10 dpa. It is, therefore, predicted that this alloy will retain decent fracture toughness to this dose level because of such high necking ductility.

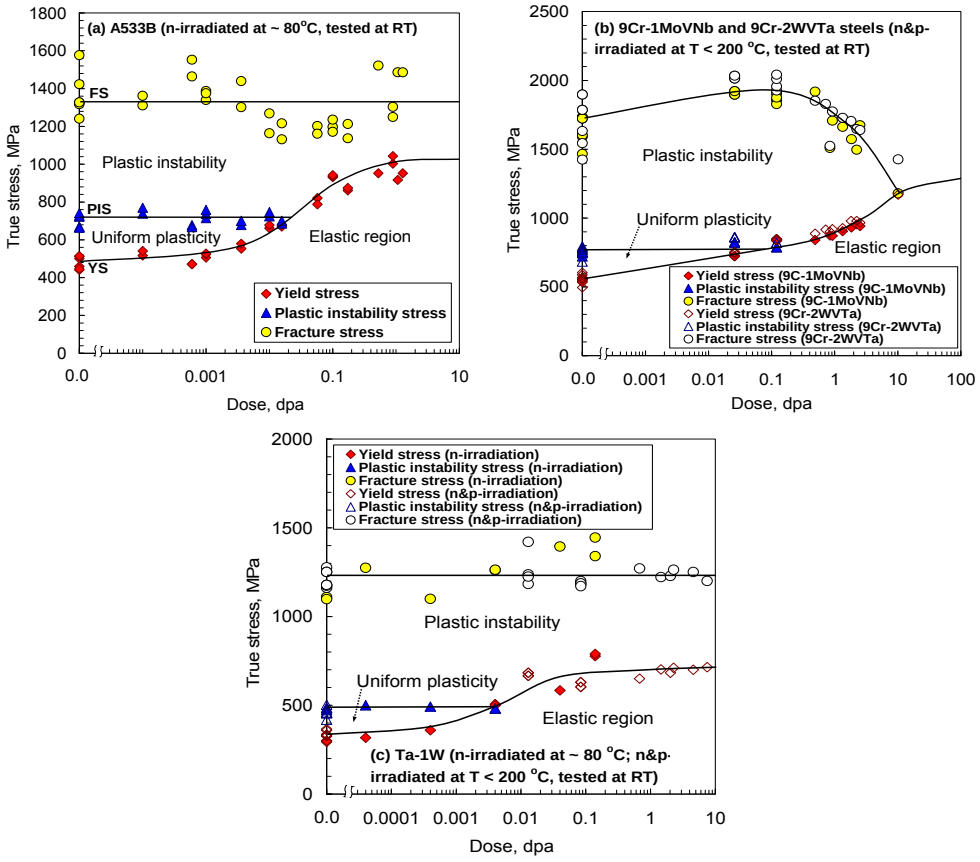

Figure 1. Deformation mode maps for bcc alloys after low temperature irradiation: (a) A533B, (b) 9Cr-1MoVNb and 9Cr-2WVTa, and (c) Ta-1W.

Comparing the sizes of the deformation regions in Fig 1, the deformation mode maps for these bcc materials are characterized by a relatively large plastic instability region and a narrow uniform deformation region. This reflects the common characteristics of bcc metals such as relatively high necking ductility and low strain-hardening rate or low strain-hardening exponent. Deformation maps for other pure bcc metals are presented in Figs. 2(a) – 2(f). In Fig. 2(a) high purity Fe shows rather mild hardening in YS. PIS value is constant at about 320 MPa until the PIS line intersects the YS-dose curve at about 0.2 dpa. Although the FS shows large scatter in the dose range of 0 – 0.79 dpa, the dose dependence is not evident in this range. The average FS is about 490 MPa and is about 1.5 times the average PIS. In keeping with this low FS/PIS ratio, the relative size of unstable plasticity region is smaller than those in the bcc steels described above.

As seen in Figs. 2(b) and 2(c), the map for low-carbon arc-cast wrought molybdenum (LCAC Mo) is a typical one for annealed bcc metal, while the map for sintered-and-wrought PM Mo has the features of a highly embrittled material. In both maps an increase of YS with dose is not observed until the dose reaches 0.001 dpa. Then the YS of LCAC Mo starts to increase until it saturates (or decrease slightly) above 0.1 dpa, while the YS of PM Mo starts to decrease due to severe embrittlement. In the LCAC Mo, both the PIS and FS are constant over the explored dose range. Fig. 2(c) indicates that the FS of PM Mo before irradiation, 860 MPa, is already much below the possible maximum fracture stress for the arc-cast pure Mo, ~1400 MPa, and the FS after irradiation continues to decrease with dose. It is observed in Figs. 1(b) and 2(c) that the FS value decreases with dose or with the degree of embrittlement. Grain boundary embrittlement is known as the main embrittlement mechanism of PM Mo and its alloys [34,35], and no abrupt drop of fracture stress was found in this study. This might indicate that the grain boundaries are

gradually weakening with dose. As a result, the map for this embrittled material has small regions of both stable and unstable deformations.

Other bcc refractory metals, Nb, V, and Ta, have similar maps to the earlier bcc maps, Figs. 2(d) – 2(f). Among these metals Nb has a relatively large uniform plasticity region due to its high strain-hardening capability. V and Ta show embrittlement at the highest doses, 0.69 and 0.14 dpa, respectively (only the ISIS Ta among the three pure Ta metals broke in a brittle mode at the dose). Both of these refractory metals have small uniform plasticity regions and much larger unstable plasticity regions, reflecting their low uniform ductility and high necking ductility. For V and Ta, the doses to plastic instability at yield are noticeably low, about 0.001 dpa, although the FS/PIS ratios are on the high side among the bcc metals, and therefore, most of their total plasticity occurs during necking.

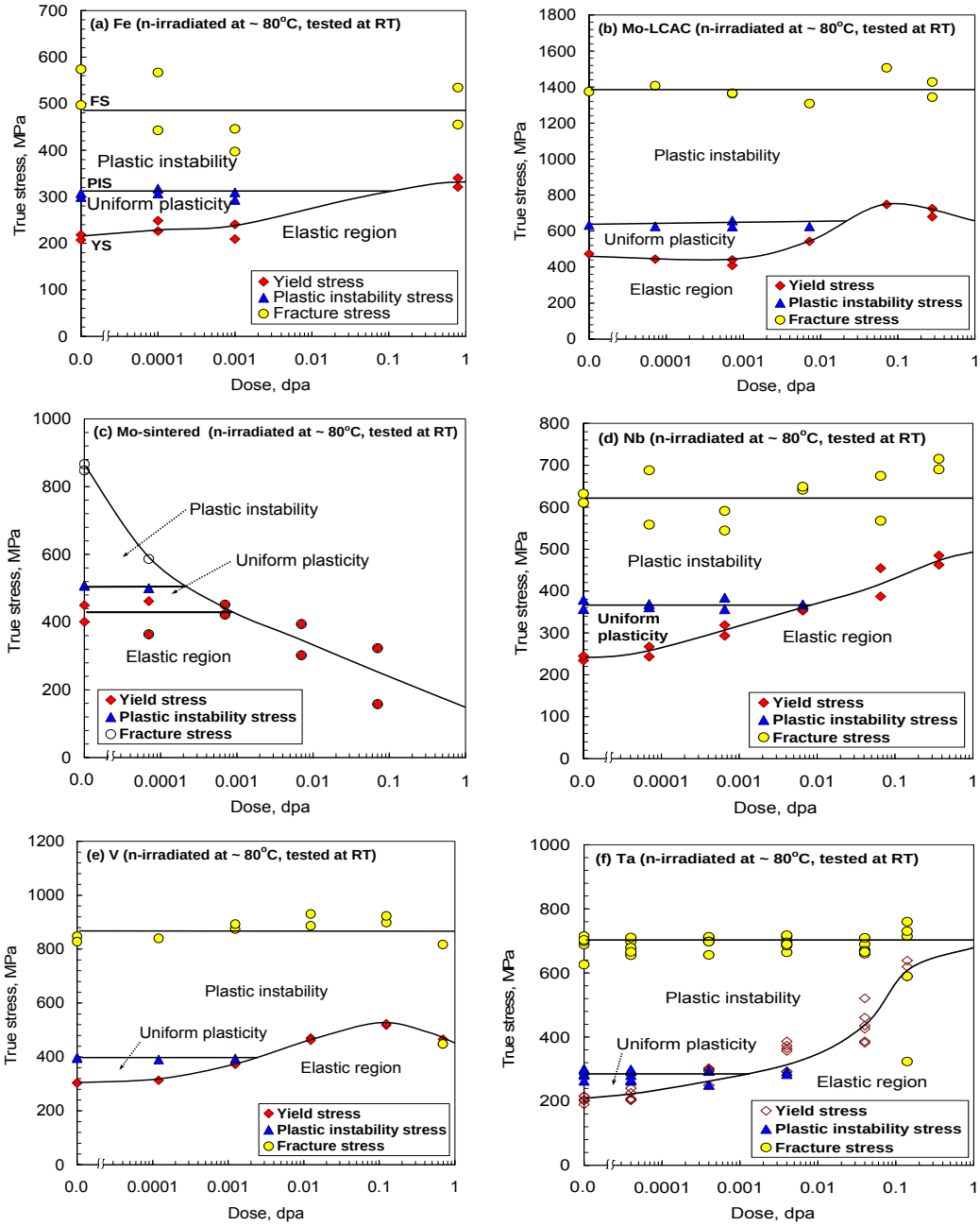

Figure 2. Deformation mode maps for pure bcc metals after low temperature irradiation: (a) Fe, (b) LCAC Mo, (c) sintered Mo, (d) Nb, (e) V, and (f) Ta (all Ta cases).

Maps for fcc materials

Figs. 3(a) – 3(d) present the maps for fcc alloys: annealed 316 and 316LN austenitic stainless steels [23] and solution annealed (SA) and precipitation hardened (PH) IN718 alloy. The PIS and FS values for the annealed alloys are nearly independent of dose, and the span between YS and PIS values before irradiation is wide; the YS values are in the range 230 – 320 MPa and the PIS values in the range 900 – 1300 MPa. This results in large uniform plasticity regions, almost as large as their plastic instability regions, and much larger than the uniform plasticity regions in the bcc metals. In the IN718-PH, however, the PIS decreases with dose in the middle dose range of 0.001 – 0.1 dpa and becomes close to the YS curve. Consequently, this precipitation-hardened material has a relatively small uniform deformation region. It is notable that the YS of this second phase hardened material is nearly stagnant over the test dose range.

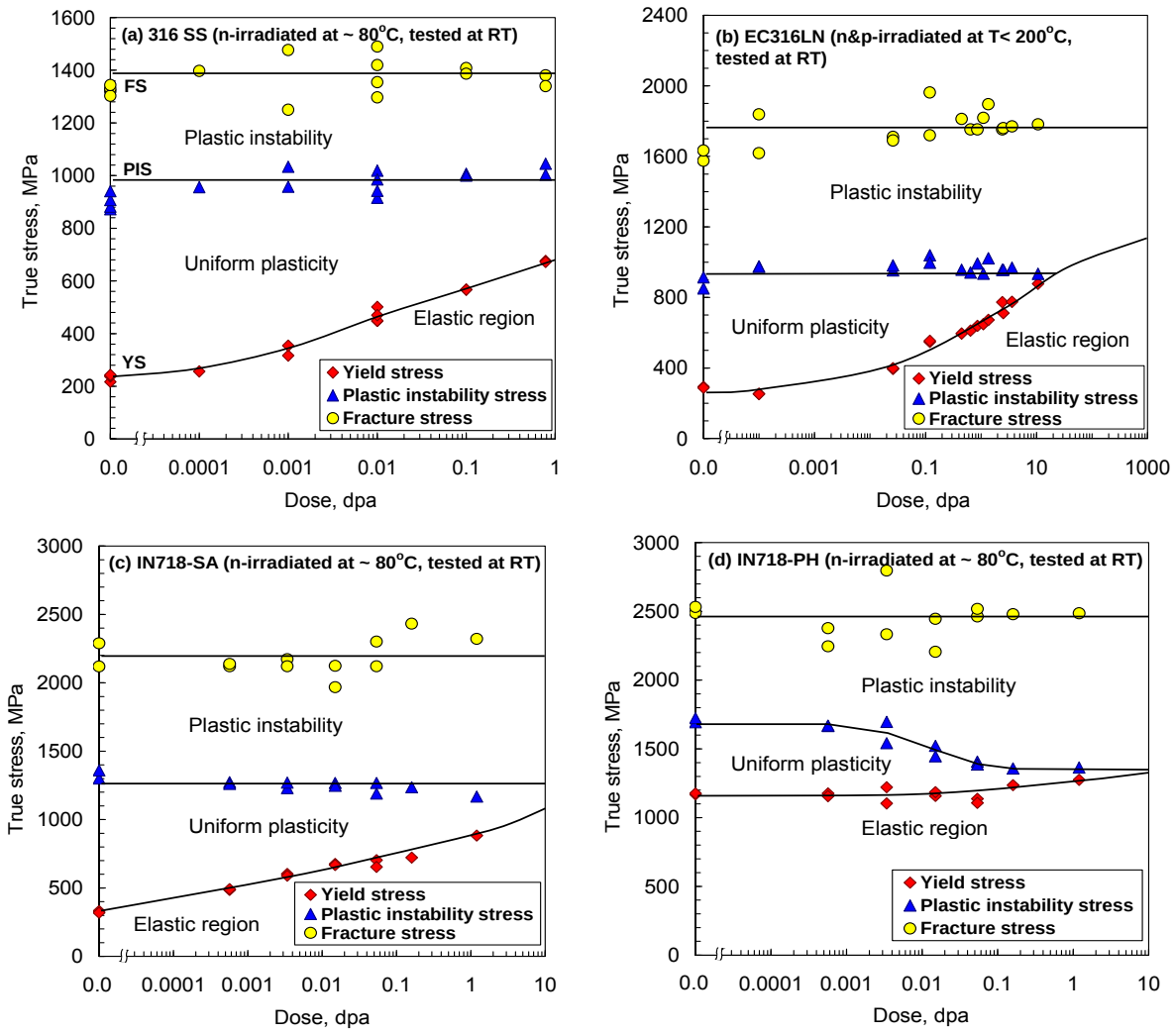

Figure 3. Deformation mode maps for fcc alloys after low temperature irradiation: (a) 316, (b) EC316LN, (c) IN718-SA, and (d) IN718-PH.

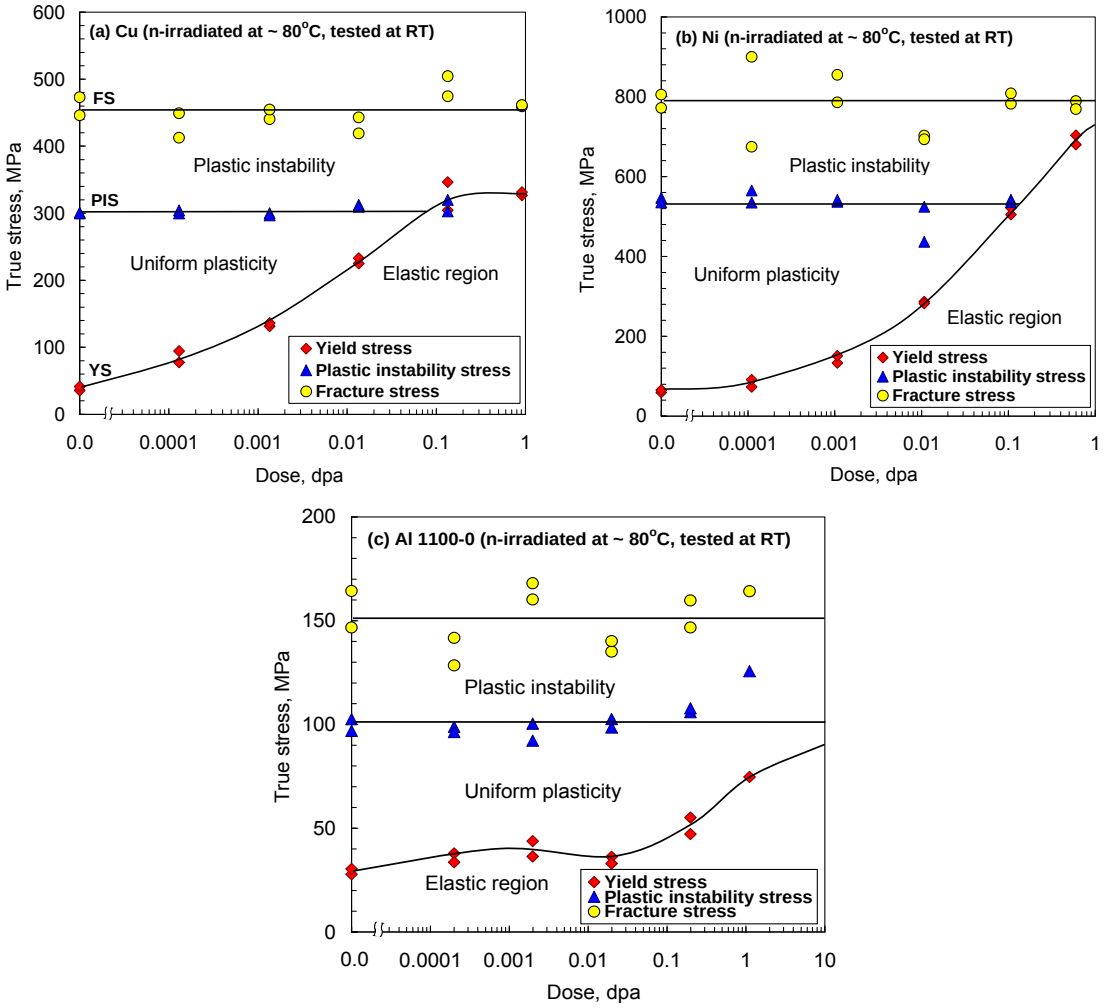

Figure 4. Deformation mode maps for pure fcc metals: (a) Cu, (b) Ni, and (c) Al.

It is also worth noting that the precipitation (or aging) heat treatment increased the YS of IN718-SA more than 3.7 times while it increased the PIS and FS just about 24% and 12%, respectively. These contrasting behaviors between IN718-SA and IN718-PH must be related to differences in microstructural changes occurring during irradiation. The IN718-SA is a single phase, solid solution-hardened material, while in the IN718-PH a high strength composite microstructure is developed during thermal aging by precipitation of spheroidal γ' ($Ni_3(Ti,Al)$) and disk-shaped γ'' (Ni_3Nb) phases in the fcc matrix [12,36]. Dissolution of the hard γ' and γ'' phases in IN718-PH during irradiation at low temperature is claimed to be responsible for holding the yield stress nearly constant with dose [12]. TEM images of the γ' and γ'' phases lost some of their intensity after irradiation to 0.1 dpa with protons and neutrons as disordering occurred in the second phases [36]. At a dose of 0.6 dpa, all evidence of the γ' and γ'' precipitates disappeared from diffraction patterns. Softening from these phase changes was presumably counterbalanced to a large extent by generation of radiation-induced point defect clusters, with a net effect of little change in flow stress [12].

Large uniform plasticity regions are also observed in the elemental fcc metals, Al, Cu, and Ni, Figs. 4(a) – 4(c). This is believed to result from the high strain-hardening capability of annealed fcc metals. Particularly in Cu and Ni, the PIS values are 7 – 9 times higher than their YS values before irradiation. The magnitude of irradiation hardening also extraordinarily high in those two metals; the maximum yield

stresses reached 8 – 11 times the YS values before irradiation. This provides evidence for the assertion that the dislocation tangles accumulated by plastic strain can resemble the damage structure produced by low temperature irradiations [37]. In the commercial grade Al, however, relatively lower hardening is observed, more comparable to those of annealed fcc alloys. Characteristics of necking deformation seem to be similar for all three metals; the distance between the FS-dose and PIS-dose curves are narrower than those in most of the bcc metals. In general, the soft fcc metals are characterized by high strain hardening but relatively rapid progress of necking when it commences.

Maps for hcp materials

Two datasets for Zircaloy-4 (Zr-4) are grouped into one map, Fig. 5(a), and cover a wide dose range of 0 – 24.6 dpa. This map has characteristics of bcc alloys, showing a relatively small uniform plasticity region and a large plastic instability region. The FS shows a small dose-dependence; it increases slightly with dose in the dose range 0 – 2 dpa and then it starts to decrease. As in the tempered martensite steels, this decrease of FS with dose is believed to be caused by a gradual approach of embrittlement. It is observed, however, that the YS is far below the FS even at the highest dose, 24.6 dpa. This implies that the Zr-4 experience a complete embrittlement only at a very high dose. As with the bcc and fcc metals, the PIS for Zr-4 does not show any dose dependence. For the dataset of Zr-4, the average PIS values for respective doses were in the range 500 – 530 MPa and the average FS values in the range 1050 – 1150 MPa; these stress values fall in narrow ranges although the data are obtained from different types of tensile specimens.

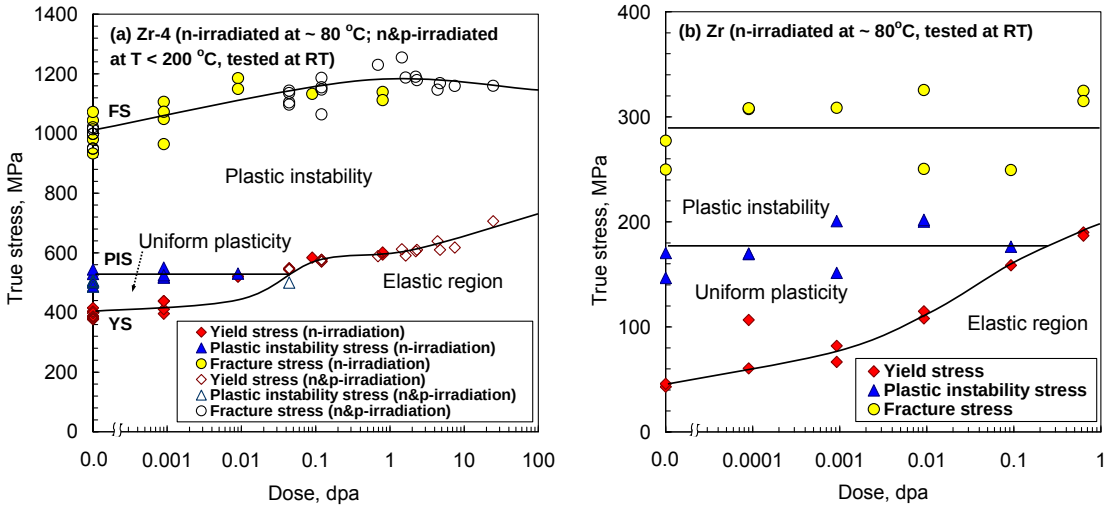

Figure 5. Deformation mode maps for hcp metals: (a) Zr-4 and (b) pure Zr.

Pure Zr is one of the softest materials in the test matrix, along with Al-1100 and Cu. The size of the uniform plasticity region in Zr is comparable to its unstable plasticity region, and the relative sizes of these deformation regions are similar to those of the low strength fcc metals. The PIS and FS of Zr are dose independent in the dose range 0 – 0.8 dpa although they show large scatters. The average PIS and FS values are much lower than those for Zr-4 alloy: 176 and 285 MPa, respectively.

Dose dependence of true strain parameters

Uniform strain and fracture strain data are presented in Fig. 6(a) to 6(c) for selected bcc, fcc, and hcp materials, respectively. In Fig. 6(a) it is observed that the fracture strains for bcc metals are in the range 0.8 – 1.5 before irradiation and start to decrease with dose after 0.001 – 0.1 dpa, while uniform strains never reach 0.2. As implied also in the stress-based deformation maps with the small uniform deformation region and large unstable deformation region, these bcc metals can be characterized by their relatively low uniform strains and predominantly large necking strains. Fracture strain remains almost unchanged over a relatively lower dose range and then started to decrease with dose; in A533B steel, for example, it decreased with dose above 0.001 dpa, and in 9Cr steels above about 0.1 dpa.

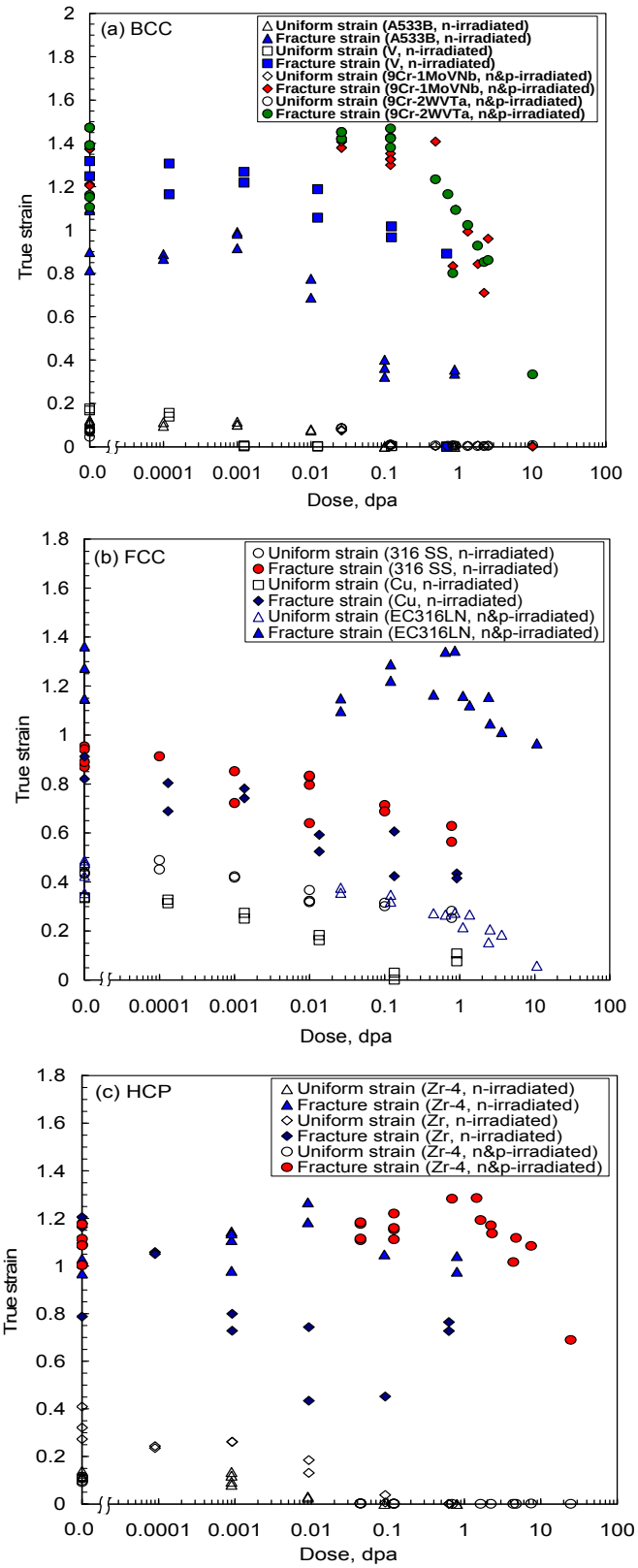

Figure 6. Dose dependence of true strain parameters for (a) bcc, (b) fcc, and (c) hcp materials.

In fcc metals, Fig. 6(b), the uniform strains are relatively higher than those for bcc metals, but fracture strains are similar to those for bcc metals. Also, the uniform and fracture strains for Cu, which is one of the softest materials, tend to be lower than those of stainless steels over the test dose range. As a group, the fcc materials are actually no more ductile than the other materials of different crystal types when compared in terms of true fracture strain. Many fcc metals grouped as highly ductile materials are possibly in an inadequate classification which overly relies on engineering strain terms such uniform and total elongations. The elongation during necking is a much shortened version of true necking strain, influenced largely by the degree of strain localization in the neck. It is also seen that the fracture strains of EC316LN are much higher than those of the standard 316 stainless steel although their uniform strains are nearly on the same trend line. It is believed that the addition of nitrogen in the EC316LN material has decreased its stacking fault energy, and thereby increased its tendency for twinning. In EC316LN the true stress during necking (> 900 MPa) is higher than the twinning stress for the steel, ~ 600 MPa, and therefore, twinning is a common deformation mechanism [38-42]. It is known that such mechanical twinning can increase strain-hardening capability and delay deformation localization and failure [24]. This observation also reminds that a true stress or true strain parameter reflecting both stable (uniform) and unstable deformations should be a consideration when an improved mechanical property is observed.

Fig. 6(c) shows that the dose dependences of the true strains for hcp metals are similar to those of bcc metals. For both pure metals and alloys, the uniform strains decrease to zero at about 0.1 dpa. The fracture strain of Zr-4 is maintained at about 1 up to about 10 dpa; it tends to decrease from about 1 dpa. No zero fracture strain or complete embrittlement was observed in the dataset. The pure zirconium actually shows lower fracture strains than the alloy although its uniform strains are higher. The amount of necking deformation is smaller in the softer pure metal. Before they decreased the fracture strains for these hcp metals were in the range of 0.8 – 1.2, similar to the bcc and fcc materials in Figs. 6(a) and 6(b). It may be a significant finding that the fracture strain is not strongly dependent on crystal structure; it seems to depend more on alloying and heat treatment.

The dose to plastic instability at yield

Since a simple increase of yield stress usually reduces uniform ductility [9], irradiation hardening almost always results in the loss of uniform ductility before embrittlement and eventually eliminates all ductility. It was found that engineering tensile curves showed necking at yield whenever the YS was higher than the dose-independent PIS [23-25,27]. This PIS criterion for plastic instability was also applied to other materials hardened by other types of defects such as dislocation tangles produced by cold working [29]. Thus, it is worth evaluating a parameter that can measure the critical amount of defect accumulation for the moment when the YS reaches the PIS. For irradiated materials, such a critical dose parameter D_C was named the dose to plastic instability (or prompt necking) at yield [24]. In the maps [27], the D_C values are graphically determined at the doses when the YS versus dose curve intercepts the PIS versus dose line. This dose parameter can be regarded as a lifetime for mechanical stability since the materials will show unstable plastic deformation above dose D_C. The D_C values are listed in Table 2, along with the data from earlier work [30,24]. Note that the D_C values beyond the irradiation dose ranges were obtained by extrapolation, and are tentative.

In bcc materials, D_C values ranged from ~0.001 to 0.2 except one pure Fe, which has an outstanding value of 6 dpa for the critical dose [24]. The large difference between the D_C values for the two pure irons is possibly due to their YS difference, which may be related to impurity levels. The YS values prior to irradiation were 213 and 104 MPa, respectively, for the Fe of case 12 and the other pure Fe [24], while their PIS values were similar at about 300 MPa. The bainitic and ferritic/martensitic steels have D_C values in the range of 0.015 – 0.12, which are relatively low when compared to the pure irons but are high when compared to the refractory metals whose values are always below 0.02. It was not possible to determine D_C for the molybdenum produced by powder metallurgy (PM) because of its prompt embrittlement and abnormal tensile behavior. The irradiation responses of the hcp metals, zirconium and Zircaloy-4, are similar to those of bcc metals: 0.004 and 0.009 dpa were obtained for Zircaloy-4 and 0.09 dpa for pure zirconium.

The fcc materials have relatively high D_C values in agreement with the general observation that the fcc materials have higher resistance to irradiation when compared to other crystal types; no D_C value was below 0.1 dpa. All the austenitic steels, cases 20 – 28, and the austenitic IN718 alloy, cases 32 and 33, show very high critical doses of at least 5 dpa. The aluminum alloys and the pure metals, Cu and Ni, have much smaller D_C values: 0.12 to 0.15 dpa. As indicated in the dose-dependence curves of YS and PIS, the critical dose D_C depends on how fast the irradiation hardening ($\Delta\sigma_{YS}$) progresses to bridge the difference that previously existed between the two stresses before irradiation. The deformation maps show that the fcc metals have generally wider uniform deformation regions compared to the bcc and fcc metals. This explains the result that the fcc metals generally take longer irradiation time or dose to reach their PIS values, indicating that in a ductile material its total work-hardening capability matters in the irradiation hardening process.

Table 2. List of the doses, D_C , to cause plastic instability at yield

Case # [Ref. #]	Material	Dose Range, dpa	D_C, dpa
1	A533B	0 - 0.89	0.02
[24]	A533B	0 - 1.2	0.015
2	A533B	0 - 1.28	0.02
[24]	3Cr-3WV	0 - 1.2	0.025
[24]	9Cr-1MoVNb	0 - 1.2	0.034
[24]	9Cr-2VWTa	0 - 1.2	0.054
[24]	9Cr-2WV	0 - 1.2	0.054
3,4	9Cr-2VWTa	0 - 10.2	0.12
5,6	Mod. 9Cr-1MoVNb	0 - 10.2	0.09
7,8,9	Ta-1W	0 – 7.52	0.005
10,11	Ta-10W	0 – 25.23	<0.01
12	Fe	0 - 0.79	0.2
[24]	Fe	0 - 1.07	6
13	Mo (LCAC)	0 – 0.28	0.02
14	Mo (PM)	0 – 0.07	>0.0007
15	Nb	0 - 0.37	0.007
16	V	0 - 0.69	0.0017
17,18,19	Ta	0 – 0.14	0.015
20	316	0 - 0.78	27
[24]	316	0 - 1.2	35
[24]	316LN	0 - 1.2	40
21,22	EC316LN	0 - 10.7	22
23,24	AL6XN	0 - 10.7	17
25,26	HTUPS316	0 - 10.7	5
27	Fe-21Ni-16Cr (R)	0 – 11.28	>11.28
28	Fe-21Ni-16Cr (S)	0 – 11.28	>11.28
29	Al1100-0	0 – 1.11	>1
30	Al6061-Ann	0 – 0.14	>>0.14
31	Al6061-T651	0 – 0.14	>0.14
32	IN718-PH	0 – 1.2	~10
33	IN718-SA	0 – 1.2	>10
34	Cu	0 - 0.92	0.12
35	Ni	0 - 0.6	0.15
36	Zr-4	0 - 0.8	0.009
37,38	Zr-4	0 - 24.6	0.004
39	Zr	0 - 0.63	0.09

Dose independence of strain-hardening behavior

As is displayed repeatedly on in the deformation mode maps [27], the PIS-dose and FS-dose lines are mostly parallel to each other if there is no embrittlement or phase change. This is an expected result from the conclusion of earlier works that the strain-hardening behavior at a given stress is nearly dose independent [23-24,27]. Figs. 3(a) to 3(c) present full true stress-true strain curves for A533B steel, EC316LN stainless steel, and Zircaloy-4, representing bcc, fcc, and hcp materials, respectively (the same curves up to onset of necking were presented in reference [24]). Here, the true stress-true strain curves up to onset of necking were obtained from tensile tests, and then the curves for the necking deformation were drawn by extending the uniform deformation curves to fracture by setting their strain-hardening rates at the PIS values. For each material, the curves for irradiated specimens were shifted along the curve for the unirradiated specimen in the positive strain direction until the irradiated YS intercepted the curve for the unirradiated specimen. As a reminder, the true stress in the unstable deformation region beyond the onset of necking (the straight lines extended to fracture in Fig. 3) is the principal stress component in the tensile direction, and consequently is slightly higher than the equivalent stress [31-33]. Thus, as assumed in the calculation (equation 2), the true stress-true strain curves after yield are close to each other. This close coincidence indicates that irradiation increases only the yield stress without significantly changing strain-hardening behavior afterwards [23,24,33]. An important outcome of this conclusion is that the loss in uniform elongation that accompanies irradiation hardening is not due to an irradiation-induced change in strain hardening behavior. It is caused simply because less strain is required to raise the heightened flow stress to the level of the unaltered plastic instability stress where necking begins.

No apparent embrittlement was observed in these three materials within the test dose ranges; if such embrittlement had occur it would have shortened the curves without changing their slopes or strain-hardening rates [23,33]. Therefore, in metals where no phase change occurs during irradiation, the irradiation effect on true stress-true strain curves can be described as: 1) increases in yield stress and no significant effects on subsequent plastic deformation, and 2) If embrittlement by non-ductile failure occurs, the fracture stress will decrease. These deductions confirm our earlier conclusion [9] that the ductility loss by low temperature irradiation is mostly due to the increase of yield stress, not to a decrease of strain-hardening rate. It can therefore be said that low temperature irradiation narrows the deformation window defined between yield stress and fracture stress. This view challenges the widely-held belief that the loss of uniform ductility after irradiation, prior to necking, is related to a reduction of strain-hardening rate or to the softening effect due to the clearance of radiation-induced defects by glide dislocations [21,30,42-53]. That belief is based largely on reading changes directly from the engineering tensile curves, or by comparing true stresses at a given strain.

Radiation-induced defect clusters such as dislocation loops, stacking fault tetrahedra, and other grown-in dislocations [1-4,45-53] have all dislocation characters such as displacement vectors and stress fields, and hence, they should produce resistance forces to dislocation glide in a similar manner to the strain hardening by dislocation tangles in nonirradiated materials [24]. This should result in similarity of irradiation hardening and strain hardening. Others [37,54-56] have reported the near-invariance of strain-hardening behavior after irradiation. They found that the strain-hardening portions of the flow curves for bcc materials after irradiation to various doses were very similar if compared at the same stress, and that they could be superimposed on the curve for unirradiated material by shifts along the strain axis.

Such near invariance of strain-hardening behavior after irradiation is considered as an unexpected phenomenon if we take into account the fact that the microscopic plastic deformation mechanism usually changes from uniform to localized deformation mode with increasing dose. Localized deformation mechanisms are dislocation channeling, and mechanical twinning. Channeling is found in most metallic materials [21,30,42,46-56]. Twinning is common in hcp, in some bcc metals at cryogenic temperatures, and in low-stacking fault energy materials like austenitic stainless steels [33,42,38-41,57-62]. In a channel a significant drop of local shear stress should occur because of defect clearance in the early stage of channel formation [42,45-53,59]. In twinning of stainless steels, which is developed by a successive glide of partial dislocations on consecutive slip planes, the stress to glide the first partial dislocation is greater

than that for the second and further partial dislocation because only movement of the first dislocation is needed to form the new stacking fault [40,57-59]. Both of these microscopic localization mechanisms can produce softening effects. However, a few earlier studies have shown that the change in deformation mechanism does not significantly affect macroscopic strain-hardening behavior if compared at the same true stresses [23,24,37,54-56,59]. In fact, the microscopic strain localization is believed to be a common phenomenon under any high stress deformation [24]. The localized (channeled) deformation has been reported for many nonirradiated but prestrained metals such as pure copper [50-53], molybdenum [45,60, 61] aluminum [62]. In these results, macroscopic strain-hardening rates were positive despite observation or prediction of localized (channeled) deformation. This implies that microscopic strain localization may coexist with more homogenous bulk deformation without causing significant macroscopic softening.

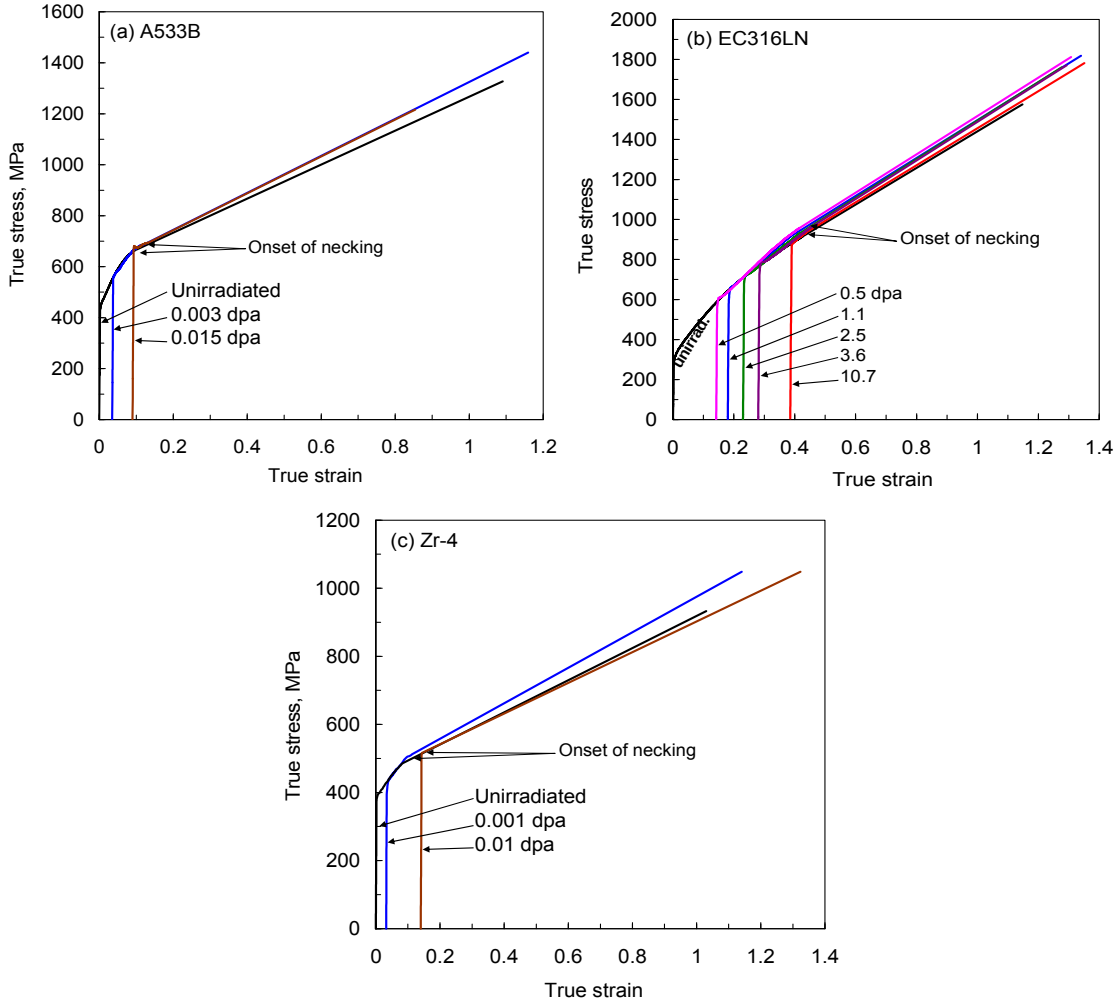

Figure 7. True stress-true strain curves extended to fracture: (a) A533B after neutron irradiation, (b) EC316LN after irradiation in spallation condition, and (c) Zr-4 after neutron irradiation.

A simplified theoretical model in terms of long-range back stress hardening [59,63] was offered to account for this concurrence of local and homogenous plastic deformation. It was devised to explain the strain-hardening behavior during strain localization in irradiated materials. Calculation results showed that in a localized band the local stress lowered by an initial localization process returned quickly to a stress level as high as those in adjacent regions, and the average stress continued to increase as the long-range back stress built up. The residual dislocations at each channel-grain boundary intercept could account for the strain-hardening rates as high as those for the microscopically-uniform deformation by dislocation tangling. This result states that the relatively-short range hardening stress from dislocation

tangling in uniform deformation is replaced by the long-range stress hardening as the plastic deformation is microscopically localized [63].

Linearity between true stress parameters

Since the two true stress parameters, PIS and FS, are nearly dose-independent in certain dose ranges, it should be possible to use the averages of the PIS and FS values as material constants for characterizing deformation of a material or a material group [25]. Also, the yield stress of nonirradiated material, YS(0), is a key property parameter for the reference material. In this section, therefore, an attempt is made to find any consistent behavior such as linearity between those parameters which can characterize material groups or crystal types. Hereafter, the three parameters, YS(0), PIS, and FS, indicate their average values.

As indicated on the macroscopic deformation maps, the strain-hardening capability of a metallic material is directly dependent on the interval between YS and PIS, and hence it is believed that the stress ratio, PIS/YS(0), is an effective parameter to present the capability. The PIS/YS(0) ratios are calculated and presented in Fig. 8 (see Table 3 for the values for individual materials). Fig. 8 displays two roughly linear lines, indicating that the materials can be classified into two groups. The first is a group of high strain-hardening capability with PIS/YS(0) ratios ranging from 3.3 – 8.4. The average PIS/YS(0) ratio was about 3.9 for this materials group, which is given as the slope of the linear line for the group. All annealed fcc metals and pure Zr (open square) belong to this materials group. Since a hcp metal (Zr) is included in this materials group, and the fcc alloys In718-PH and the hcp Zr-4 fall on the line for the bcc group, crystal type is not a sufficient criterion to determine whether a material belongs to a particular group; other factors must play a role.

The second materials group, or lower slope group, includes all bcc pure metals and alloys (thin dashed line), hcp alloy (Zr-4) (solid line), and precipitation hardened fcc alloys such as Al6061-T651 and IN718-PH (open squares). This materials group with lower strain-hardening capability showed PIS/YS(0) ratios ranging from 1.1 to 1.6, with an average of 1.4; which is just slightly above 1/3 of the average ratio for the softer materials group. The materials showing such low PIS/YS(0) ratios correspond to those with narrow uniform deformation region in the maps, Figs. 1 – 5.

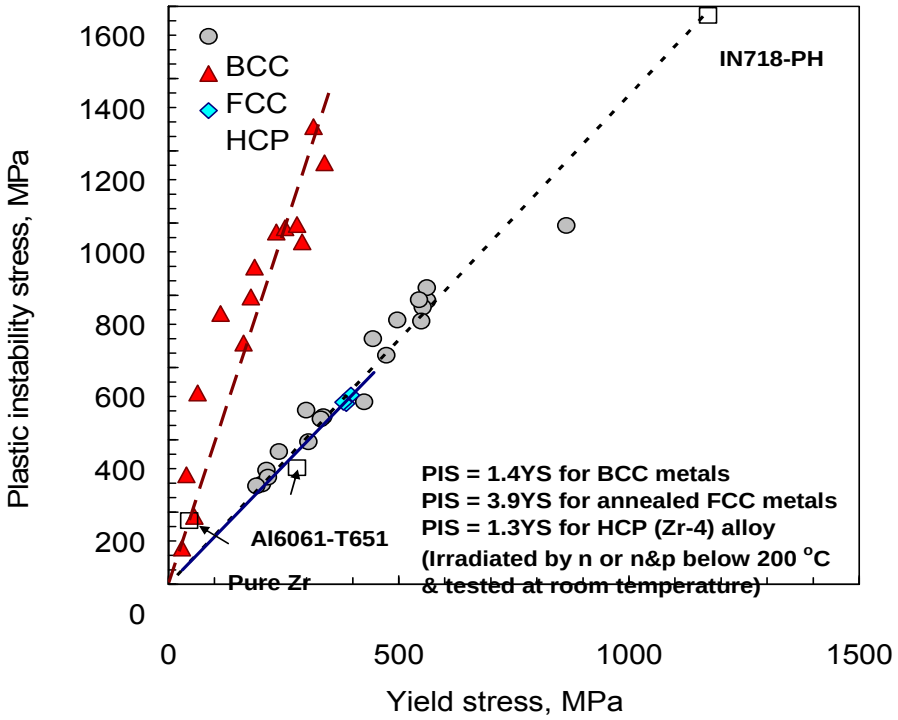

Figure 8. Linear relationship between YS and PIS.

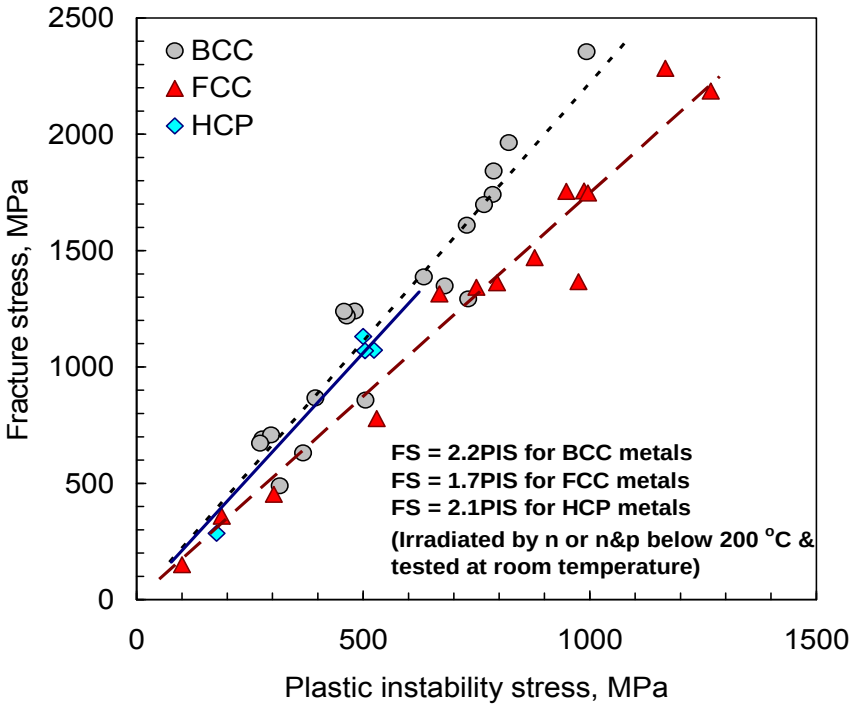

Figure 9. Linear relationship between PIS and FS.

The PIS and FS represent the start and finish of necking deformation, and the necking plasticity and strain-hardening rate will determine the ratio between the two parameters. It was concluded earlier that the strain-hardening rate was nearly independent of dose, and moreover, remained at the PIS during unstable deformation if no embrittlement occurred [23,33]. It is expected therefore that this simple hardening behavior during necking leads to a simple relationship between PIS and FS [23]. Indeed, the calculation results in Fig. 9 display a strong linear relationship between PIS and FS. The FS/PIS ratios for A533B steel, 9Cr steels, and pure refractory metals (Mo, Nb, and V) ranged from 1.7 to 2.4. Also, slightly higher values of 2.2 – 2.7 were calculated for the pure tantalums and the alloys Ta-1W and Ta-10W. Fe showed the lowest value,1.5, among the bcc metals tested.

Slightly lower FS/PIS ratios were calculated for fcc pure metals and alloys than for bcc and hcp metals, and the variations among fcc metals were also lower. The FS/PIS ratios for fcc metals ranged from 1.4 to 2.0. While the FS/PIS ratios obtained for hcp Zircaloy-4 (2.0, 2.1, and 2.3) are similar to those of typical bcc alloys, the ratio for pure Zr (1.6) is close to the lower end values of bcc metals. Thus, the fitting line given for hcp metals in Fig. 5 (solid line) almost coincides with the thin dashed line for bcc materials. As given in Fig. 5, the averages of FS/PIS ratios, or the slopes of fitting lines, were 2.2, 1.7, and 2.1, respectively, for the bcc, fcc, and hcp groupings. It is worth noting that among the tested materials the spread of the FS/PIS ratios over the range 1.4 – 2.7 is smaller than that of the PIS/YS(0) ratios in the range 1.1 – 8.4. This indicates that among the metallic materials less variation in the behavior of unstable tensile deformation is predicted than in the behavior of uniform deformation. This should be because the necking deformation is relatively unaffected by irradiation [25].

The strong relationship between PIS and FS should make it possible to predict FS from PIS, or vice versa. For most ductile materials, this predictability may be retained until the material is embrittled at high doses: for example, lower than 1 dpa for refractory metals, ~1 dpa for non-austenitic steels, and higher than 10 dpa for austenitic stainless steels. Considering that any experimental measurement on necking deformation is difficult, this predictability can be significant for practical use because it enables the prediction of whole necking and fracture process with reasonable accuracy from the uniform deformation

data and PIS value which can be easily obtained from routine tensile tests. If non-ductile failure occurs, however, the FS values decrease with dose and the linearity between PIS and FS will be broken. After a complete embrittlement, or when fracture occurs before the applied stress reaches the yield stress, the FS values may show wider statistical variation and become more sensitive to specimen conditions such as surface flaws, inclusions, geometrical irregularities, etc. No consistent correlation between PIS and FS is expected in such a circumstance.

Table 3. True stress data and stress ratios

Case #	Material	Dose Range, dpa	YS (at 0 dpa/at highest dose), MPa	Average PIS, MPa	Average FS, MPa	PIS/YS(0)	FS/PIS
1	A533B	0 – 0.89	497 / 1023	732	1292	1.5	1.8
2	A533B	0 – 1.28	444 / 952	680	1348	1.5	2.0
3*	9Cr-2WVTa	0 – 10.15	562 / 1170	786	1741	1.4	2.2
4	9Cr-2WVTa	0 – 0.12	561 / 846	821	1964	1.5	2.4
5*	9Cr-1MoVNb	0 – 10.15	552 / 1183	767	1698	1.4	2.2
6	9Cr-1MoVNb	0 – 0.12	544 / 839	788	1842	1.4	2.3
7	Ta-1W	0 – 0.14	299 / 783	482	1276	1.6	2.6
8	Ta-1W	0 – 7.52	336 / 715	464	1219	1.4	2.6
9	Ta-1W	0 – 0.08	331 / 617	458	1239	1.4	2.7
10	Ta-10W	0 – 25.23	864 / 1483	993	2355	1.1	2.4
11	Ta-10W	0 – 0.08	549 / 940	729	1609	1.3	2.2
12	Fe	0 – 0.79	213 / 281	316	489	1.5	1.5
13	Mo (LCAC)	0 – 0.28	473 / 723	634	1387	1.3	2.2
14*	Mo (PM)	0 – 0.07	425 / -	505	857	1.2	1.7
15	Nb	0 – 0.37	240 / 474	368	630	1.5	1.7
16*	V	0 – 0.69	304 / 457	395	867	1.3	2.2
17	Ta (Aesar-1)	0 – 0.14	203 / 595	278	636	1.4	2.3
18	Ta (Aesar-2)	0 – 0.14	216 / 629	297	802	1.4	2.7
19	Ta (ISIS)	0 – 0.14	191 / 590	273	638	1.4	2.3
20	316	0 – 0.78	234 / 674	975	1367	4.2	1.4
21	EC316LN	0 – 10.67	290 / 877	948	1755	3.3	1.9
22	EC316LN	0 – 0.12	253 / 551	987	1757	3.9	1.8
23	AL6XN	0 – 10.67	279 / 980	996	1747	3.6	1.8
24	AL6XN	0 – 0.12	339 / 629	1167	2284	3.4	2.0
25	HTUPS316	0 – 4.0	179 / 791	795	1362	4.4	1.7
26	HTUPS316	0 – 0.12	187 / 517	878	1470	4.7	1.7
27	Fe-21Ni-16Cr(R)	0 – 11.28	113 / 641	750	1343	6.6	1.8
28	Fe-21Ni-16Cr(S)	0 – 11.28	163 / 591	668	1314	4.1	2.0
29	Al 1100-0	0 – 1.11	29 / 97	100	151	3.5	1.5
30	Al 6061-Ann	0 – 0.14	56 / 72	188	359	3.4	1.9
31	Al 6061-T651	0 – 0.14	279 / 279	323	629	1.2	1.9
32	IN718-PH	0 – 1.2	1172 / 1275	1575	2447	1.3	1.6
33	IN718-SA	0 – 1.2	315 / 883	1267	2186	4.0	1.7
34	Cu	0 – 0.92	39 / 329	303	453	7.8	1.5
35	Ni	0 – 0.6	63 / 692	530	778	8.4	1.5
36	Zr-4	0 – 0.8	396 / 598	524	1072	1.3	2.0
37	Zr-4	0 – 24.58	386 / 706	500	1131	1.3	2.3
38	Zr-4	0 – 0.12	380 / 574	504	1069	1.3	2.1
39	Zr	0 – 0.63	45 / 189	176	285	3.9	1.6

* Data for ductile failure only; averages excluded data from embrittled specimens.

Conclusions

The irradiation dose dependencies of the true stress parameters for bcc, fcc, and hcp pure metals and alloys were integrated into 18 deformation mode maps. Conclusions on the maps and true stress parameters are:

[1] Drawing a true stress parameter-based deformation mode map on a true stress-dose plane is an effective way of displaying the deformation data of an irradiated material. The macroscopic deformation mode maps reflect well the characteristics of irradiation effects on mechanical behaviors for individual materials or material groups.

[2] Comparing the extents of deformation regions, the uniform plasticity regions were generally large and dominant in annealed fcc metals, while the unstable plasticity regions were dominant in harder bcc and hcp metals. Large uniform deformation regions in fcc metals were attributed to their higher strain-hardening capability.

[3] The dose independencies of PIS and FS were demonstrated for all the test materials that did not exhibit a phase change or embrittlement. YS increased with dose in all the materials except the IN718-PH where a radiation-induced phase change was suspected to have interfered, as inferred by a decrease of PIS. In some materials signs of radiation-induced embrittlement were indicated by a decrease of FS with dose at high doses.

[4] No obvious dependence of fracture strains on crystal structure was observed, while uniform strains were generally larger in annealed fcc metals than in bcc or hcp metals. Alloys tended to retain fracture strains after irradiation as high as those of softer pure base metals.

[5] Comparison of true stress-true strain curves extended to fracture and overlapped at the same stresses showed that the major effect of low temperature irradiation is to increase the yield stress while not significantly changing the strain-hardening rate. Uniform ductility is shortened because less strain is required to raise the flow stress (the heightened yield stress) to the level of the plastic instability stress where necking begins. Irradiation decreases the fracture stress when non-ductile failure occurs. The insensitivity of strain hardening to irradiation was explained by the result that the relatively-short range hardening stress from dislocation tangling in uniform deformation was replaced by the longer-range stress hardening as the plastic deformation was microscopically localized.

[6] The near dose independences of PIS and FS resulted in strong linear relationships between true stress parameters: average PIS/YS(0) ratios were about 1.4, 3.9, and 1.3 for bcc metals (and precipitation hardened alloys), annealed fcc metals (and pure Zr), and hcp alloy, respectively. The FS/PIS ratios were calculated to be 2.2, 1.7, and 2.1, for bcc, fcc, hcp materials, respectively. These numbers confirm that the annealed fcc metals have larger uniform ductility but smaller necking ductility when compared to the other materials.

Acknowledgements

This research was sponsored by U.S. Department of Energy, Offices of Fusion Energy Sciences and Basic Energy Science, under Contract DE-AC05-00OR22725 with UT-Battelle, LLC. The author expresses special thanks to (Drs. R. L. Klueh and J. T. Busby) for technical reviews and thoughtful comments.

References

[1] Lee EH, Hunn JD, Hashimoto N, Mansur LK. J Nucl Mater **278** (2000) 266.
[2] Singh BN, Foreman AJE, Trinkaus H. J Nucl Mater **249** (1997) 103.
[3] Victoria M, Baluc N, Bailat C, Dai Y, Luppo MI, Schaublin R, Singh BN. J Nucl Mater **276** (2000) 114.
[4] Eldrup M, Singh BN, Zinkle SJ, Byun TS, Farrell, K. J Nucl Mater **307-311** (2002) 912.
[5] Singh BN, Edwards DJ, Toft P. J Nucl Mater **238** (1996) 244.
[6] Koppenaal TJ, Arsenault RJ. Metals Rev **157** (1971) 175.
[7] Pawel JE, Rowcliffe AF, Alexander DJ, Grossbeck ML, Shiba K. J Nucl Mater **233-237** (1996) 202.
[8] Farrell K, Byun TS. J Nucl Mater **296** (2001) 129.
[9] Byun TS, Farrell K, Lee EH, Hunn JD, Mansur LK. J Nucl Mater **298** (2001) 269.
[10] Byun TS, Farrell K, Lee EH, Mansur LK, Maloy SA. James MR, WR Johnson. J Nucl Mater **303** (2002) 34.
[11] Farrell K, Byun TS. J Nucl Mater **318** (2003) 274.
[12] Byun TS, Farrell K. J Nucl Mater **318** (2003) 292.
[13] Byun TS, Hashimoto N. Nucl & Engi Tech **38** (2006) 619.
[14] Zinkle SJ, Lucas GE. Fusion Mater Semiann Prog Rep **DOE/ER-0313/21** (2003)101.
[15] Ashby MF. Acta Met **20** (1972) 887.
[16] Stocker RL, Ashby MF. Rev Geophys Space Phys **11** (1973) 391.
[17] Ashby MF. The Microstructure and Design of Alloys, The Inst Metals and The Iron and Steel Inst, London, **2** (1973) 8.
[18] Frost HJ, Ashby MF. Deformation-Mechanism Maps, Pergamon Press, 1982.
[19] Ashby MF, Materials Selection in Mechanical Design, Pergamon Press, 1992.
[20] Okada A, Kanao K, Yoshiie T, Kojima S. Mater Trans JIM **30** (1989) 265.
[21] Farrell K, Byun TS, Hashimoto N. J Nucl Mater **335** (2004) 471.
[22] Byun TS, Hashimoto N, Farrell K. J Nucl Mater **351** (2006) 303.
[23] Byun TS. J Nucl Mater **361** (2007) 239.
[24] Byun TS, Farrell K. Acta Mater **52** (2004) 597.
[25] Byun TS, Farrell K, M. Li, Acta Mater **56** (2008) 1056.
[26] Farrell K, Byun TS, Hashimoto N. Mapping flow localization processes in deformation of irradiated reactor structural alloys, Oak Ridge National Lab., **ORNL/TM-2003/63** (2003).
[27] Byun TS, Farrell K, Li M, Acta Mater. **56** (2008) 1044.
[28] Farrell K, Byun TS. Tensile properties of candidate SNS materials after irradiation in two neutron areas in the LANSCE accelerator, Oak Ridge National Lab. **SNS/TR-211** (2001).
[29] Byun TS, Hashimoto N, Farrell K. Acta Mater **52** (2004) 3889.
[30] Byun TS, Farrell K. J Nucl Mater **326** (2004) 86.
[31] Bridgman PW. Studies in Large Plastic Flow and Fracture, McGraw-Hill, NY, 1952.
[32] Ling Y, AMP J Tech **5** (1996) 37.
[33] Scheider I, Brocks W, Cornec A. Trans. ASME **126** (2004)70.
[34] Bryhan AJ. Welding Research Council Bulletin **312** (1986).
[35] Miller MK, Kenik EA, Mousa MS, Russell KF, Bryhan AJ. Scripta Mater **46** (2002) 299.
[36] Hashimoto N, Hunn JD, Byun TS, Mansur LK. J Nucl Mater **318** (2003) 300.
[37] DiMelfi RJ, Alexander DE, Rehn LE. J Nucl Mater **252** (1998)171.
[38] Lee EH, Byun TS, Hunn JD, Yoo MH, Farrell K, Mansur LK. Acta Mater **49** (2001) 3269.
[39] Lee EH, Yoo MH, Byun TS, Hunn JD, Farrell K, Mansur LK. Acta Mater **49** (2001) 3277.
[40] Byun TS. Acta Mater **51** (2003) 3036.
[41] Byun TS, Lee EH, Hunn JD. J Nucl Mater **321** (2003) 29.

[42] Byun TS. Hashimoto N, Farrell K. J Nucl Mater **349** (2006) 251.
[43] Tucker RP, Wechsler MS, Ohr SM, J Appl Phys **40** (1969) 400.
[44] Li M, Hashimoto N, Byun TS, Snead LL, Zinkle SJ, J. of Nucl. Mater **367-370** (2007) 817.
[45] Luft A. Pro Mater Sci **35** (1991) 97.
[46] Smidt FA, Jr. Dislocation Channeling in Irradiated Metals, Naval Res. Lab., Washington D.C. **NRL Report 7078** (1970).
[47] Wechsler MS. Dislocation Channeling in Irradiated and Quenched Metals (Ch.2), in: The Inhomogeneity of Plastic Deformation, Amer. Soc. for Metals, Metals Park, Ohio, (1971) 19-54.
[48] Makin MJ, Sharp JV. Phys Stat Sol **9** (1965)109.
[49] Sharp JV. Phil Mag **16** (1967) 77.
[50] Sharp JV. Acta Metal **22** (1974) 449.
[51] Hashimoto N, Byun TS, Farrell K, Zinkle SJ. J Nucl Mater **336** (2005) 225.
[52] Hashimoto N, Byun TS, Farrell K. J Nucl Mater **329-333** (2004) 947.
[53] Hashimoto N, Byun TS, Farrell K. J Nucl Mater **351** (2006) 295.
[54] Mogford IL, Hull D. J Iron & Steel Inst **201** (1963) 55.
[55] Ohr SM. Scripta Metall **2** (1968) 213.
[56] Van Osch EV, DeVries MI. J Nucl Mater **271&272** (1991)162.
[57] Jin Z, Bieler TR. Phil Mag A **72** (1995) 1201.
[58] Jin Z, Bieler TR. Phil Mag A **71** (1995) 925.
[59] Byun TS, Hashimoto N. J ASTM Inter **4** (2007).
[60] Brenner B, Luft A. Mater Sci Engi **52** (1982) 229.
[61] Ritschel C, Luft A, Schulze D. Kristall und Technik **13** (1978) 791.
[62] Cottrell AH, Stokes RJ. Proc Roy Soc **A233** (1955) 17.
[63] Byun TS, Hashimoto N. J Nucl Mater **354** (2006)123